






Testing High-energy Emission Models for Blazars with X-Ray Polarimetry

Abel L. Peirson¹ , Ioannis Liodakis² , and Roger W. Romani¹ ¹ Kavli Institute for Particle Astrophysics and Cosmology, Stanford University, Stanford, CA 94305, USA; alpv95@stanford.edu² Finnish Centre for Astronomy with ESO, University of Turku, Vesilinnantie 5, FI-20014, Finland

Received 2022 March 25; revised 2022 April 21; accepted 2022 April 24; published 2022 May 25

Abstract

Both leptonic and hadronic emission processes may contribute to blazar jet emission; which dominates in blazars' high-energy emission component remains an open question. Some intermediate synchrotron peaked blazars transition from their low- to high-energy emission components in the X-ray band making them excellent laboratories to probe both components simultaneously, and good targets for the newly launched Imaging X-ray Polarimetry Explorer (IXPE). We characterize the spectral energy distributions for three such blazars, CGRaBS J0211+1051, TXS 0506+056, and S5 0716+714, predicting their X-ray polarization behavior by fitting a multizone polarized leptonic jet model. We find that a significant detection of electron synchrotron dominated polarization is possible with a 300 ks observation for S5 0716+714 and CGRaBS J0211+1051 in their flaring states, while even 500 ks observations are unlikely to measure synchrotron self-Compton (SSC) polarization. Importantly, nonleptonic emission processes like proton synchrotron are marginally detectable for our brightest intermediate synchrotron peaked blazar (ISP), S5 0716+714, during a flaring state. Improved IXPE data reduction methods or next-generation telescopes like eXTP are needed to confidently measure SSC polarization.

Unified Astronomy Thesaurus concepts: X-ray active galactic nuclei (2035); X-ray telescopes (1825); Relativistic jets (1390); Galaxy jets (601); Polarimetry (1278); Polarimeters (1277); BL Lacertae objects (158)

1. Introduction

Blazars are active galactic nuclei whose relativistic jets are oriented at an angle θ_{obs} within a few degrees, typically $<15^\circ$ (Liodakis et al. 2018), from an observer on Earth. This results in the relativistically boosted emission from the jet to outshine the host galaxy. The jet's observed multiwavelength emission, from radio to γ -rays, is characterized by two broad components. The low-energy component is attributed to synchrotron emission from primary jet electrons, while the high-energy component is still unknown with inverse-Compton (IC) scattering or hadronic processes (proton synchrotron, pion cascades, etc.) as the current favored mechanisms (Blandford et al. 2019). Blazars are often classified by the peak frequency (ν_{S_1}) of the low-energy component (Abdo et al. 2010). Here we focus on the intermediate synchrotron peaked (ISP) blazars, whose synchrotron emission peaks in optical/UV and have their spectral energy distributions (SEDs) dropping toward eventual high-energy component dominance in the hard X-ray/ γ -ray band. In particular, we focus on a subclass of ISPs whose X-ray emission lies in the valley formed by the combination of the two spectral components.

While the origin of the high-energy component is still unknown, the recent launch of the Imaging X-ray Polarimetry Explorer (IXPE; Weisskopf et al. 2021) offers a new diagnostic tool to probe the jet physics, composition, and acceleration of particles. In Liodakis et al. (2019) we used a multizone jet model (Marscher 2014; Peirson & Romani 2018, 2019) and optical polarization results from the RoboPol survey (Blinov et al. 2021) to make predictions for the X-ray polarization degree of blazars. In a synchrotron self-Compton (SSC) scenario, we expect substantial polarization from the electron

synchrotron and much lower polarization levels from the Compton component. On the other hand, the polarization degree of proton synchrotron and synchrotron from hadron initiated pair cascades is expected to be much higher than that of IC emission and comparable to that of the primary electron synchrotron component. Interestingly, as one observes further out on the electron synchrotron cutoff tail, fewer jet emission zones have sufficient particle energies and Doppler factors to produce the detected radiation—this means that there is decreased polarization angle (PA) averaging between emission zones and thus a larger net synchrotron polarization degree and higher variability (Peirson & Romani 2018, 2019). Polarization measurements in the transition region between low- and high-energy components can thus be a powerful tool to probe not only for the high-energy emission processes, but also the jet and magnetic field structure. Coincidentally, recent hybrid (also known as leptohadronic) blazar models for the high-energy neutrino emission suggest the existence of subdominant synchrotron components from proton-initiated pair cascades that might only be detectable in the transition valley where any primary lepton emission is minimized (e.g., Gao et al. 2019). All of the above suggest that ISPs, whose transition regions lie in the 1–10 keV band, are particularly attractive targets for current and future X-ray polarization missions.

We have identified three such sources, namely CGRaBS J0211+1051, TXS 0506+056, and S5 0716+714. CGRaBS J0211+1051 and S5 0716+714 are first-year IXPE targets, while CGRaBS J0211+1051 and TXS 0506+056 are potential neutrino emitters (IceCube Collaboration et al. 2018; Hovatta et al. 2021). Our goal is twofold: (1) to understand the polarization behavior of the jet across the transition region; and (2) to make predictions for IXPE and future missions to understand the high-energy emission signatures from blazars. In Section 2 we describe the data and jet models, in Section 3 we make predictions for IXPE, and in Section 4 we discuss our findings.

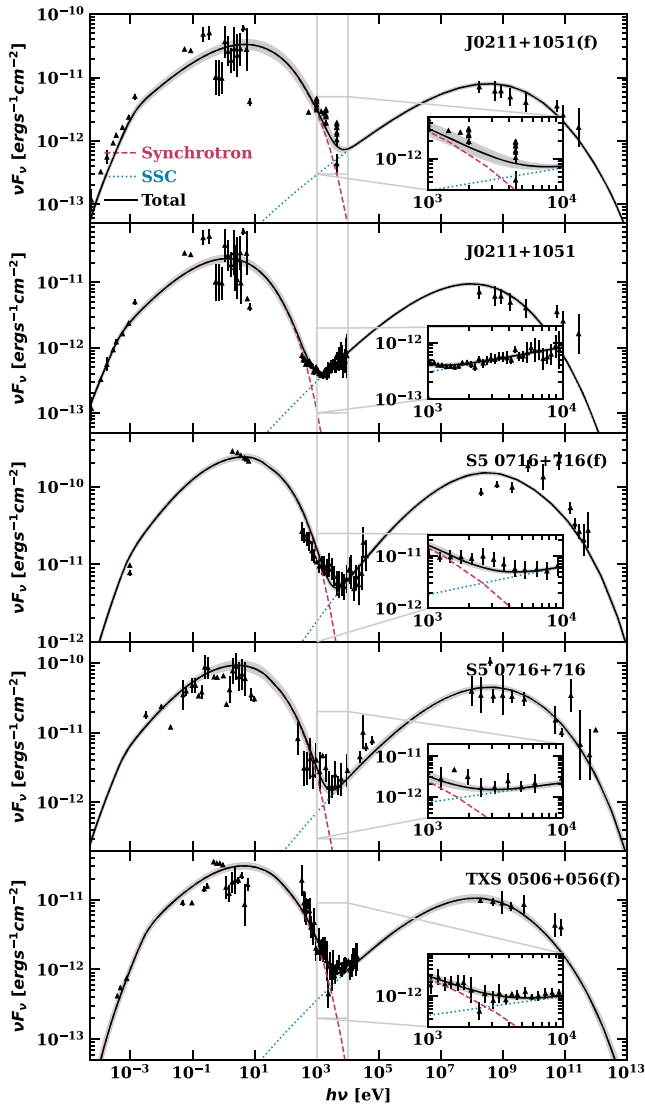


Figure 1. Polarized leptonic jet model fits to all blazars and states. “(f)” denotes a flaring state. Black traces show the expected total SED for the best-fit jet parameters. Gray shaded regions around the black trace show 1σ model deviations due to different random magnetic field zones. Vertical gray lines denote IXPE’s sensitive band, 1–10 keV, and insets show close-ups of this region.

2. Multiwavelength Observations and Modeling

The non-X-ray multiwavelength data for all sources are taken from the Space Science Data Center archive.³ The data are not contemporaneous and include both flaring and quiescent periods of each source. Since the latter may allow improved polarization measurements, we analyze quiescent and flaring data separately. We bin the observations in frequency bins of 0.1 dex and treat the resulting SED as an “average” SED of the source in the given state. Examples are shown in Figure 1.

For the X-ray observations we used publicly available Neil Gehrels Swift Observatory (Swift), NuSTAR, and XMM-Newton data from the High Energy Astrophysics Science Archive Research Center (HEASARC) browse interface. The X-ray observations for the source in normal and flaring (f)

Table 1
X-Ray Spectral Parameters

Name	N_{H}	Γ_2	Γ_1
CGRaBS J0211+1051	0.16	1.18 ± 0.19	2.68 ± 0.4
TXS 0506+056	0.25	1.83 ± 0.2	3.88 ± 1.0
S5 0716+714	0.031	1.56 ± 0.33	2.36 ± 0.14

Note. The N_{H} values are given in units of $\times 10^{22} \text{ cm}^{-2}$.

states are drawn from the following date ranges: CGRaBS J0211+1051(f) (MJD 55260–55886), CGRaBS J0211+1051 (MJD 59250), S5 0716+714(f) (MJD 57046), S5 0716+714 (MJD 54864–55920), and TXS 0506+056(f) (MJD 58025). For CGRaBS J0211+1051 in quiescence we augment with a new ~ 65 ks XMM-Newton observation (AO-19, ID number: 0861840101, MJD 59250). All Swift data used were contemporaneous (within 1–2 days) with exposures from one of the other facilities. The data were processed using the standard HEASARC tools and recommended analyses.

Previous fits to these data have typically used absorbed broken power-law models for TXS 0506+056 (IceCube Collaboration et al. 2018) and S5 0716+714 (Wierzecholska & Siejkowski 2016). Instead, we fit the extracted spectra, using Xspec, with a more physically motivated model: the sum of two power-law components, subject to absorption by a Galactic neutral hydrogen column N_{H} . For CGRaBS J0211+1051, the publicly available Swift snapshots did not provide sufficient signal-to-noise to unambiguously determine the shape of the 1–10 keV spectrum. We thus tried three models, a single power law, a power law with an exponential cutoff, and a sum of two power laws. We then used the Akaike information criterion to select the model that best describes the data. Again the sum of two power laws is preferred. The best-fit model parameters are given in Table 1.

2.1. SED Modeling

Our joint SED and polarization modeling uses the polarized leptonic jet emission model developed in Peirson & Romani (2018, 2019), inspired partly by Potter & Cotter (2012) and Marscher (2014). It assumes an initial power-law electron population propagating along a relativistic conical jet. The jet cross section is divided into multiple magnetic field zones, with isotropically distributed field orientations. These magnetic fields are comoving with the jet material. Polarized synchrotron emission is self-consistently calculated as the electron population propagates and cools. SSC emission is computed, including the propagation of synchrotron photons from downstream emission into each Comptonizing zone. For quasi-spherical magnetic field zones, as often assumed in turbulent scenarios, the model resolves a decorrelation timescale (which depends on the initial jet parameters) of 0.5–5 days. This is the timescale over which steady-state jet emission is expected to fluctuate.

An important feature of this jet model is variable Doppler boosting of the zones, since those directed closest to the line of sight are increasingly dominant in the observed flux as the SED steepens (Peirson & Romani 2019). This guarantees an increasing expected polarization degree and larger polarization variability above the synchrotron peak. The X-ray SSC polarization degree is typically $\sim 0.2\text{--}0.35\times$ that of the synchrotron peak polarization; the components’ PAs are highly

³ <https://tools.ssdc.asi.it/SED/>

Table 2
Polarized Jet Model Best-fit Parameters

Name	W_j ($10^{37}W$)	E_{\max} ($10^9 eV$)	α	θ_{open} ($^\circ$)	Γ_{bulk}	B_0 ($10^{-5}T$)	θ_{obs} ($^\circ$)	A_{eq}
J0211+1051(f)	4.94 ± 0.1	13.4 ± 1.0	2.05 ± 0.01	7.16 ± 0.19	14.8 ± 0.64	5.04 ± 0.2	1.95 ± 0.18	0.81 ± 0.01
J0211+1051	6.48 ± 0.2	9.59 ± 0.1	1.85 ± 0.01	14.1 ± 0.35	7.23 ± 0.15	2.38 ± 0.2	2.31 ± 0.09	0.83 ± 0.02
TXS 0506+056	5.26 ± 0.5	8.03 ± 0.3	1.89 ± 0.01	4.15 ± 0.26	17.3 ± 0.42	9.63 ± 0.3	1.64 ± 0.11	0.98 ± 0.05
S5 0716+714(f)	42.4 ± 5.0	13.4 ± 3.0	1.66 ± 0.02	7.35 ± 0.62	13.2 ± 0.51	2.84 ± 0.6	2.51 ± 0.06	1.05 ± 0.02
S5 0716+714	47.3 ± 11.0	9.49 ± 1.5	1.75 ± 0.09	5.93 ± 0.84	17.0 ± 0.64	3.23 ± 1.5	4.48 ± 0.16	0.84 ± 0.13

Note. Jet power W_j , electron high-energy cutoff before exponential decay E_{\max} , electron population power-law index α , full conical jet opening angle in lab frame θ_{open} , bulk Lorentz factor Γ_{bulk} , initial magnetic field strength B_0 , jet observation angle in lab frame θ_{obs} , and initial equipartition fraction A_{eq} . (f) denotes a flaring state. The number of magnetic field zones N_{zones} is selected from [1, 7, 19, 37, 64, 128]. All blazar models shown here use 37 magnetic field zones except CGRaBS J0211+1051, which uses 19.

correlated. In this model the observed synchrotron and SSC polarization behavior depends significantly on the geometric jet parameters, such as the jet opening angle, observation angle, and Lorentz factor.

Our leptonic jet emission model is essentially independent of particle acceleration methods since it follows zones downstream of any acceleration region. The assumed “chaotic” disordered magnetic fields and relativistic boosting effects should be present in many magnetic reconnection and shock acceleration scenarios. We also assume steady-state emission, probing polarization variability by reseeding the magnetic field zones. We briefly discuss how these simplifying assumptions may be violated in other models found in the literature in Section 4.

In order to constrain our model’s jet parameters, we fit the multiwavelength SED observations of each blazar state. Due to the chaotic magnetic field zones, our model is stochastic: the same jet parameters can result in different observed SEDs. A stochastic optimization method is necessary to fit such a model to fixed observations. We use a simple variant of the cross-entropy method (Rubinstein & Kroese 2004; Kochenderfer & Wheeler 2019). At each step, this samples n sets of jet parameters from a multivariate Gaussian and refits a new Gaussian using k samples with the lowest χ^2 . Steps are repeated until convergence, when the mean and covariance matrix of the Gaussian no longer change significantly between steps. We use $n = 80$, $k = 20$. Since the multiwavelength SEDs for each blazar are not simultaneous and the true SEDs can be much more variable than the observational errors imply, we make the simplifying assumption that every observation has the same error. Our jet model has eight free parameters. We open source the code to run our model and reproduce the results (Peirson 2022).⁴

Model fit results are shown in Figure 1. Best-fit jet parameters and their respective errors are displayed in Table 2. In Figure 2 we show the predicted polarization behavior resulting from the jet model fits displayed in Figure 1. The number of magnetic field zones in the jet model is selected so that the predicted optical polarization fraction matches the median of the observations (Blinov et al. 2021) as closely as possible. Note that individual realizations of the polarization fraction can vary significantly.

It is useful to compare our polarization predictions to previous studies. Zhang et al. (2019) model TXS 0506+056 using a single zone leptonic emission model with a uniform magnetic field, matching the observed optical polarization degree with a constant polarization dilution factor. They predict

an SSC polarization degree of approximately 5% in the X-ray band, rising to 8% at MeV energies. This represents a slightly higher X-ray polarization fraction, increasing more strongly to high energy. The differences can be attributed to our multizone setup, where multiple magnetic field orientations relative to the line of sight affect the net-synchrotron-to-SSC-polarization ratio and its energy dependence (Bonometto & Saggion 1973; Peirson & Romani 2019); multizone models generally predict a lower SSC polarization degree. We note that our model also propagates synchrotron seed photons between magnetic field zones, further diluting the SSC polarization and increasing sensitivity to the jet geometry.

3. IXPE Measurement Simulations

A principal goal of IXPE ISP source measurements is to detect two different X-ray polarizations—a lower-energy, electron synchrotron dominated component and a higher-energy component. Assuming an SSC spectrum, we explore whether such a measurement is possible for each of our ISPs with typical IXPE exposures, using IXPE’s standard analysis pipeline processing over a 2–8 keV band.

Using *ixpeobssim*, IXPE’s observation simulation software (Pesce-Rollins et al. 2019), we simulate multiple 300 and 500 ks observations for each blazar state assuming polarization and flux are fixed to their expected (average) values (i.e., the black traces in Figures 1 and 2). We split the simulated 2–8 keV data into two energy bins: 2–4 and 4–8 keV, extracting the polarization fractions by estimating the Stokes parameters as in Kislat et al. (2015). Figure 3 summarizes the results.

In Figure 3, energy bins where the true polarization fraction distribution (blue, right-hand side) is fully below the minimum detectable polarization (MDP₉₉) threshold (dotted lines) cannot produce significant ($\gtrsim 3\sigma$) detection of nonzero polarization in the given exposure time. MDP₉₉ is the 99th percentile upper confidence bound on polarization fraction for an unpolarized source. Energy bins with some or all of the true polarization distribution above MDP₉₉ can have significant detections, if their actual polarization is in the upper portion of the predicted range—the measurement errors would be approximately given by the measured polarization fraction distributions for the most probable p_0 (red, left-hand side). Planned observation times for first-year IXPE ISP targets, including CGRaBS J0211+1051 and S5 0716+714, are expected to range from 200 to 400 ks.

For each blazar and state the two energy bins, 2–4 and 4–8 keV, contain different relative synchrotron and SSC contributions. Insets in Figure 1 give the relative contributions. In nonflaring states, both energy bins are almost entirely

⁴ <https://github.com/alpv95/SSCpol>

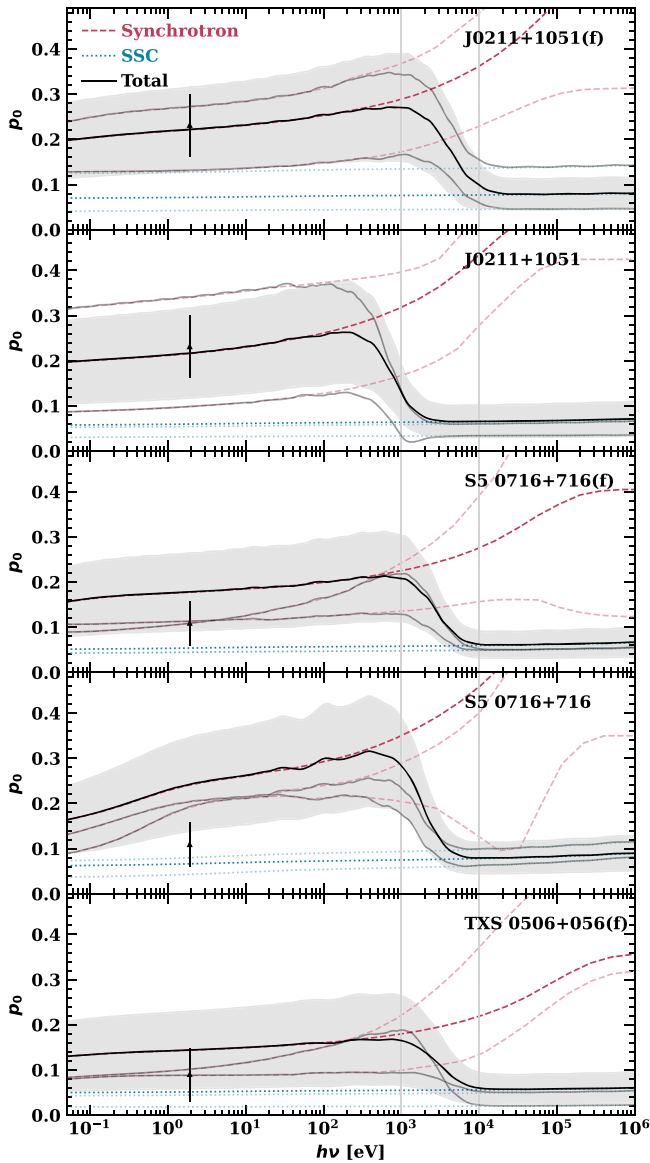


Figure 2. Leptonic (SSC) jet model polarization fraction predictions. The jet models used in each panel are the same as those in Figure 1. Black observations denote the average measured optical polarization over multiple epochs (MJD 56432–57893 for Robopol measured S5 0716+714 and J0211+1051 (Blinov et al. 2021) and MJD 58019–58267 for TXS 0506+056). Lines and shaded regions mean the same as Figure 1 with the addition of two transparent models, which represent randomly selected model realizations.

dominated by SSC emission so measurement of the synchrotron cutoff component will not be possible.

Low significance polarization fraction measurements, below MDP_{99} , are strongly biased away from $p_0 = 0$. Strict nonnegativity of p_0 forces measurement posteriors (red, Figure 3) to be asymmetric and for $\mathbb{E}(\hat{p}_0) > p_0$ (see, especially, CGRaBS J0211+1051 quiescent panel). This highlights the danger of making polarization inferences using low significance point estimates. The measurement bias can be corrected using appropriate p_0 estimators (Simmons & Stewart 1985).

4. Discussion

Under a purely leptonic (SSC) jet model for ISPs, we find that simultaneously detecting significant X-ray polarization

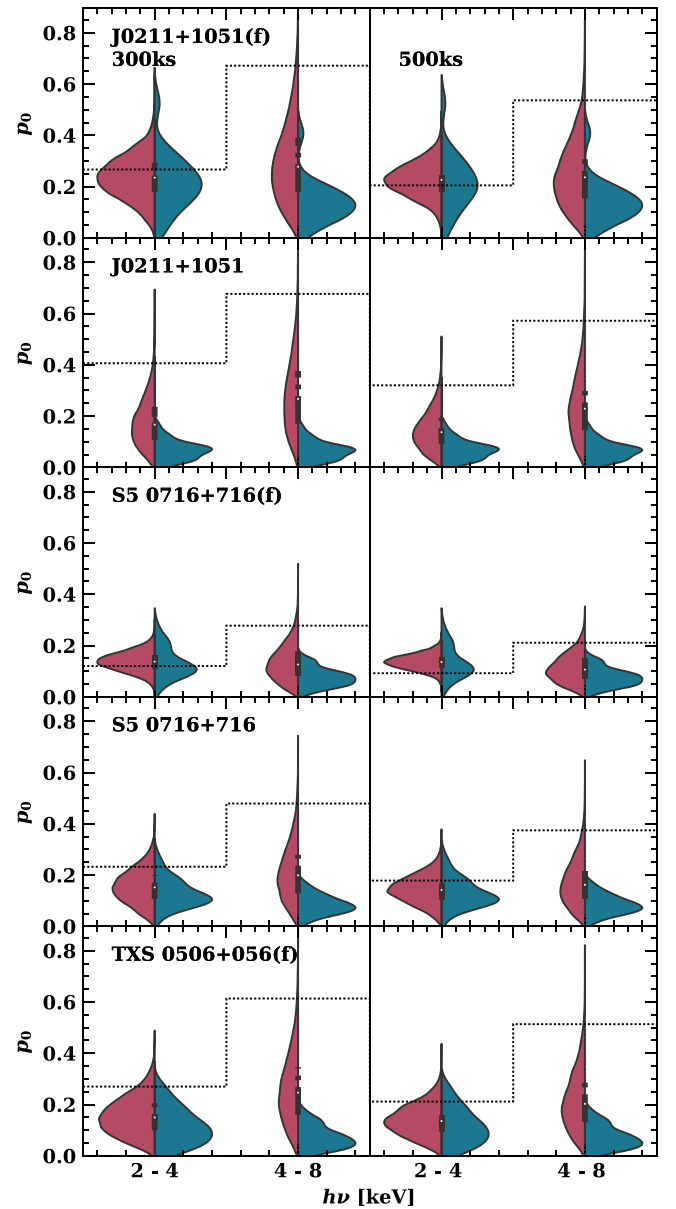


Figure 3. Violin plots of the true polarization fraction distribution (blue, left-hand side) and the measured polarization fraction distribution (red, right-hand side) for 2–4 and 4–8 keV energy bins, and 300/500 ks exposures. The distributions of true polarization fractions are extracted from our jet model fits (Figure 2) and are the same for both exposure times. Measured polarization fraction distributions assume a single observation with true polarization equal to the expected value. Dashed black traces represent the minimum detectable polarization (MDP_{99}) for each measurement bin.

from both emission components with a ≤ 500 ks IXPE observation is impossible, even considering high p_0 fluctuations (see Figure 3). For the assumptions used here, a 2.5 Ms exposure would be required to measure the median predicted SSC polarization in our brightest source, S5 0716+714, during its high state. Unfortunately, blazar polarization variability may preclude such long observation times. Optical polarization measurements (Blinov et al. 2021) suggest that blazar polarization fraction and PA can vary significantly over time periods < 500 ks. This would result in an incoherent averaging of polarization vectors leading to depolarization. Many blazar

models (Marscher 2014) including our own (Figure 2) predict polarized X-ray electron synchrotron emission to be more variable than the optical (Di Gesu et al. 2022).

If external Compton (EC) contributes significantly to a blazar’s high-energy emission component, the case for measuring its X-ray polarization becomes even more dim. EC emission is usually assumed to be unpolarized (Zhang & Bottcher 2013) since the external photon field being scattered is assumed incoherent, originating in the broad line region or accretion disk. Even a small EC contribution can make observations more difficult because $MDP_{99} \propto 1/\sqrt{N_{ph}}$. A 10% fractional EC contribution would lower Figure 3 true polarization fractions by 10% and increase required observation times for the same significance by 23%. Luckily, all three sources considered are classified as BL Lac objects, typically associated with low EC contributions. Padovani et al. (2019), however, suggest that TXS 0506+056 is an FSRQ in disguise, in which case there might be significant EC contribution to the high-energy component.

For the ISPs in flaring states, a significant polarization measurement of the synchrotron cutoff is feasible although still difficult, requiring the blazar to be in a high polarization state. Along the primary synchrotron cutoff we expect an increased expected polarization fraction and variability compared to the optical SED peak (see Figure 2) as the most Doppler-boosted magnetic field zones increasingly dominate the observed emission (Peirson & Romani 2019). Our model presents the minimal (geometry-induced) increase in polarization degree above the primary synchrotron peak; other effects may further increase the dominance of individual zones. For example, in the shock scenario particles are more efficiently accelerated when the magnetic field is aligned along the shock normal (Marscher 2014). Thus chaotic magnetic field zones will vary in their upper electron energy cutoff and that energy can correlate with the global jet geometry. The highest energy electrons contributing X-ray emission are close to the shock, where cooling is limited and the field orientation (and hence polarization) is more highly correlated. Also, Tavecchio et al. (2018) show that immediately downstream of a shock magnetic field compression increases the field perpendicular to the shock normal; this preferential alignment tends to correlate the field orientations and increase net polarization degree, although such correlation decays as turbulence develops downstream. Both these effects may increase polarization at the high-energy end of the synchrotron component, improving measurement prospects. In contrast magnetic reconnection scenarios suggest synchrotron cutoff polarization with higher variability but similar net polarization degree to the synchrotron peak emission (Tavecchio et al. 2018; Zhang et al. 2020). Thus comparing X-ray polarization to simultaneous optical polarization degree may be able to distinguish these acceleration scenarios.

Unexpectedly large high-energy component polarization arising from nonleptonic jet emission is possible and potentially detectable. Our leptonic (SSC) jet model predicts any high-energy component polarization should typically be $0.2\text{--}0.35\times$ lower than at the SED optical peak (Peirson & Romani 2019) with the decrement sensitive to the jet geometry. Of course, this ratio is variable and can occasionally fluctuate to large values >0.5 , especially if the peak polarization is low, so only multiepoch trends or long-term averages have predictive power. In the most optimistic hadronic jet scenario,

proton and secondary electron synchrotron dominate the high-energy emission component (Zhang & Bottcher 2013; Gao et al. 2019). High-energy component X-ray band polarization fractions would be similar to the SED optical peak (Figure 2), corresponding to an X-ray/optical polarization ratio of 1, extremely unlikely in a SSC-dominant leptonic emission model. Although this would provide a much needed polarization fraction boost, a two-component detection would remain out of reach, even for a ≤ 500 ks IXPE observation, for all ISPs except S5 0716+714 in its flaring state. Indeed, S5 0716+714 is the first ISP IXPE target, planned for a 300 ks observation on 2022 March 31; a significant polarization detection for both high- and low-energy components would be a promising indication of nonleptonic jet emission.

If initial IXPE observations do not detect significant polarization from either emission component in any ISPs, it will be difficult to rule out nonleptonic processes. Upper polarization fraction limits based on the MDP_{99s} in Figure 3 will be too high to make any useful inference about the polarization ratio of the two emission components, even with a strong synchrotron detection at 2–4 keV. However, the measurements’ sensitivity may be improved. Bayesian neural network analysis of IXPE data (Peirson et al. 2021; Peirson & Romani 2021) has been shown to reduce MDP_{99s} by up to 25% compared to the standard IXPE analysis pipeline, as well as increase IXPE’s effective energy band to 1–10 keV. We may also tune the energy range of the “low” and “high” energy detection windows for an individual source’s SED, improving our ability to measure or bound the two components’ p_0 . Such improved analysis could, for example, make a flaring 4–8 keV S5 0716+714 SSC polarization detection possible with a 500 ks observation—see Figure 3. Although neural network analysis is not yet in production for IXPE, a reanalysis of borderline observations could reveal missed discoveries. Looking further ahead, the effective area of future X-ray polarization mission eXTP (Zhang et al. 2018) should be 4 times larger than IXPE’s, reducing MDP_{99s} by a factor of 0.5 (Di Gesu et al. 2020). Including both improvements, simultaneous measurement of both ISP emission components with a 500 ks observation is well in scope for all the ISPs considered here.

The authors thank the anonymous referee and Dinesh Kandel for useful comments and discussions that helped improved this work. This research has made use of data and/or software provided by the High Energy Astrophysics Science Archive Research Center (HEASARC), which is a service of the Astrophysics Science Division at NASA/GSFC. Based on observations obtained with XMM-Newton, an ESA science mission with instruments and contributions directly funded by ESA Member States and NASA. This research has made use of data from the RoboPol program, a collaboration between Caltech, the University of Crete, IA-FORTH, IUCAA, the MPIfR, and the Nicolaus Copernicus University, which was conducted at Skinakas Observatory in Crete, Greece. A.L.P. is supported by the Stanford Data Science Scholars Program, NASA FINESST program (grant 80NSSC19K1407), and grant NNM17AA26C from the Marshall Space Flight Center.

Facilities: IXPE, NuSTAR, RoboPol, Swift, XMM-Newton.
Software: *ixpeobssim*, *SSCpol*.

ORCID iDs

Abel L. Peirson  <https://orcid.org/0000-0001-6292-1911>
 Ioannis Liodakis  <https://orcid.org/0000-0001-9200-4006>
 Roger W. Romani  <https://orcid.org/0000-0001-6711-3286>

References

- Abdo, A. A., Ackermann, M., Agudo, I., et al. 2010, *ApJ*, **716**, 30
 Blandford, R., Meier, D., & Readhead, A. 2019, *ARA&A*, **57**, 467
 Blinov, D., Kiehlmann, S., Pavlidou, V., et al. 2021, *MNRAS*, **501**, 3715
 Bonometto, S., & Saggion, A. 1973, *A&A*, **23**, 9
 Di Gesu, L., Ferrazzoli, R., Donnarumma, I., et al. 2020, *A&A*, **643**, A52
 Di Gesu, L., Tavecchio, F., Donnarumma, I., et al. 2022, arXiv:2201.09597
 Gao, S., Fedynitch, A., Winter, W., & Pohl, M. 2019, *NatAs*, **3**, 88
 Hovatta, T., Lindfors, E., Kiehlmann, S., et al. 2021, *A&A*, **650**, A83
 IceCube Collaboration, Aartsen, M. G., & Ackermann, M. 2018, *Sci*, **361**, 1378
 Kislak, F., Clark, B., Beilicke, M., & Krawczynski, H. 2015, *APh*, **68**, 45
 Kochenderfer, M. J., & Wheeler, T. A. 2019, *Algorithms for Optimization* (Cambridge, MA: MIT Press)
 Liodakis, I., Peirson, A. L., & Romani, R. W. 2019, *ApJ*, **880**, 29
 Liodakis, I., Romani, R. W., Filippenko, A. V., et al. 2018, *MNRAS*, **480**, 5517
 Marscher, A. P. 2014, *ApJ*, **780**, 87
 Padovani, P., Oikonomou, F., Petropoulou, M., Giommi, P., & Resconi, E. 2019, *MNRAS*, **484**, L104
 Peirson, A. 2022, alp95/SSCpol: v1.3.1, Zenodo, doi:10.5281/zenodo.6450411
 Peirson, A. L., & Romani, R. W. 2018, *ApJ*, **864**, 140
 Peirson, A. L., & Romani, R. W. 2019, *ApJ*, **885**, 76
 Peirson, A. L., & Romani, R. W. 2021, *ApJ*, **920**, 40
 Peirson, A. L., Romani, R. W., Marshall, H. L., Steiner, J. F., & Baldini, L. 2021, *NIMPA*, **986**, 164740
 Pesce-Rollins, M., Lalla, N. D., Omodei, N., & Baldini, L. 2019, *NIMPA*, **936**, 224
 Potter, J., & Cotter, G. 2012, *MNRAS*, **423**, 756
 Rubinstein, R. Y., & Kroese, D. P. 2004, *Monte-carlo Simulation (Information Science and Statistics)* (Berlin: Springer-Verlag)
 Simmons, J. F. L., & Stewart, B. G. 1985, *A&A*, **142**, 100
 Tavecchio, F., Landoni, M., Sironi, L., & Coppi, P. 2018, *MNRAS*, **480**, 2872
 Weisskopf, M. C., Soffitta, P., Baldini, L., et al. 2021, arXiv:2112.01269
 Wierzcholska, A., & Siejkowski, H. 2016, *MNRAS*, **458**, 2350
 Zhang, H., & Bottcher, M. 2013, *ApJ*, **774**, 18
 Zhang, H., Fang, K., Li, H., et al. 2019, *ApJ*, **876**, 109
 Zhang, H., Li, X., Giannios, D., et al. 2020, *ApJ*, **901**, 149
 Zhang, S., Santangelo, A., Feroci, M., et al. 2018, *SCPMA*, **62**, 29502